

Registration No.

#24852



An Orthotropic Model for Composite Materials in EPIC

UNCLASSIFIED: Distribution Statement A. Approved for Public Release

June 2014

U.S. Army Tank Automotive Research,
Development, and Engineering Center
Detroit Arsenal
Warren, Michigan 48397-5000

Report Documentation Page

Form Approved
OMB No. 0704-0188

Public reporting burden for the collection of information is estimated to average 1 hour per response, including the time for reviewing instructions, searching existing data sources, gathering and maintaining the data needed, and completing and reviewing the collection of information. Send comments regarding this burden estimate or any other aspect of this collection of information, including suggestions for reducing this burden, to Washington Headquarters Services, Directorate for Information Operations and Reports, 1215 Jefferson Davis Highway, Suite 1204, Arlington VA 22202-4302. Respondents should be aware that notwithstanding any other provision of law, no person shall be subject to a penalty for failing to comply with a collection of information if it does not display a currently valid OMB control number.

1. REPORT DATE 06 JUN 2014	2. REPORT TYPE Technical Report	3. DATES COVERED 20-12-2012 to 15-06-2014	
4. TITLE AND SUBTITLE An Orthotropic Model for Composite Materials In EPIC		5a. CONTRACT NUMBER W56HZV-13-C-0047	
		5b. GRANT NUMBER	
		5c. PROGRAM ELEMENT NUMBER	
6. AUTHOR(S) Stephen Beissel		5d. PROJECT NUMBER 18.19018	
		5e. TASK NUMBER	
		5f. WORK UNIT NUMBER	
7. PERFORMING ORGANIZATION NAME(S) AND ADDRESS(ES) Southwest Research Institute, 5353 Wayzata Blvd., Suite 607, Minneapolis, MN, 55416		8. PERFORMING ORGANIZATION REPORT NUMBER 18.19018/006	
9. SPONSORING/MONITORING AGENCY NAME(S) AND ADDRESS(ES) U.S. Army TARDEC, 6501 East Eleven Mile Rd, Warren, Mi, 48397-5000		10. SPONSOR/MONITOR'S ACRONYM(S) RDECOM-TARDEC/RDTA-RS	
		11. SPONSOR/MONITOR'S REPORT NUMBER(S) #24852	
12. DISTRIBUTION/AVAILABILITY STATEMENT Approved for public release; distribution unlimited			
13. SUPPLEMENTARY NOTES The views, opinion, and/or findings contained in this report are those of the authors and should not be construed as an official Department of the Army position, policy, or decision, unless so designated by other documents.			
14. ABSTRACT Orthotropic plasticity and failure were added to the existing orthotropic elasticity model in EPIC for the purpose of modeling impact loading of composites. Plasticity is represented by the Hill yield function with an associated flow rule, and failure is indicated when any component of the plastic natural-strain tensor exceeds its critical value. Example computations are included to demonstrate the model and its applicability to composites under ballistic impacts.			
15. SUBJECT TERMS Composites, fiber-reinforced polymers, orthotropic plasticity, orthotropic failure, delamination, computational plasticity			
16. SECURITY CLASSIFICATION OF:			17. LIMITATION OF ABSTRACT Public Release
a. REPORT unclassified	b. ABSTRACT unclassified	c. THIS PAGE unclassified	
			18. NUMBER OF PAGES 37
19a. NAME OF RESPONSIBLE PERSON			

UNCLASSIFIED

*An Orthotropic Model for
Composite Materials in EPIC*

Stephen R. Beissel

Southwest Research Institute
5353 Wayzata Blvd., Suite 607
Minneapolis, MN 55416

Contract: W56HZV13C0047WD001

SwRI[®] Report No. 18.19018/006

Prepared for:

U. S. Army RDECOM-TARDEC
AMSRD-TAR-R
Warren, MI 48397-5000

June 2014

UNCLASSIFIED: Distribution A: Approved for public release.

UNCLASSIFIED

UNCLASSIFIED

UNCLASSIFIED

REPORT DOCUMENTATION PAGE			<i>Form Approved</i> OMB No. 0704-0188	
Public reporting burden for this collection of information is estimated to average 1 hour per response, including the time for reviewing instructions, searching data sources, gathering and maintaining the data needed, and completing and reviewing the collection of information. Send comments regarding this burden estimate or any other aspect of this collection of information, including suggestions for reducing this burden to Washington Headquarters Service, Directorate for Information Operations and Reports, 1215 Jefferson Davis Highway, Suite 1204, Arlington, VA 22202-4302, and to the Office of Management and Budget, Paperwork Reduction Project (0704-0188) Washington, DC 20503.				
PLEASE DO NOT RETURN YOUR FORM TO THE ABOVE ADDRESS.				
1. REPORT DATE (DD-MM-YYYY) 06/06/2014		2. REPORT TYPE Final Technical		3. DATES COVERED (From - To) 12/20/2012 – 06/15/2014
4. TITLE AND SUBTITLE An Orthotropic Model for Composite Materials In EPIC			5a. CONTRACT NUMBER W56HZV-13-C-0047	
			5b. GRANT NUMBER	
			5c. PROGRAM ELEMENT NUMBER	
6. AUTHOR(S) Stephen R. Beissel			5d. PROJECT NUMBER 18.19018	
			5e. TASK NUMBER	
			5f. WORK UNIT NUMBER	
7. PERFORMING ORGANIZATION NAME(S) AND ADDRESS(ES) Southwest Research Institute 5353 Wayzata Blvd., Suite 607 Minneapolis, MN 55416			8. PERFORMING ORGANIZATION REPORT NUMBER 18.19018/006	
9. SPONSORING/MONITORING AGENCY NAME(S) AND ADDRESS(ES) US Army Tank-Automotive Research, Development, and Engineering Center, Warren, MI 48397-5000			10. SPONSOR/MONITOR'S ACRONYM(S) RDECOM-TARDEC/RDTA-RS	
			11. SPONSORING/MONITORING AGENCY REPORT NUMBER	
12. DISTRIBUTION AVAILABILITY STATEMENT Distribution A: Approved for public release; unlimited distribution.				
13. SUPPLEMENTARY NOTES The views, opinion, and/or findings contained in this report are those of the authors and should not be construed as an official Department of the Army position, policy, or decision, unless so designated by other documents.				
14. ABSTRACT Orthotropic plasticity and failure were added to the existing orthotropic elasticity model in EPIC for the purpose of modeling impact loading of composites. Plasticity is represented by the Hill yield function with an associated flow rule, and failure is indicated when any component of the plastic natural-strain tensor exceeds its critical value. Example computations are included to demonstrate the model and its applicability to composites under ballistic impacts.				
15. SUBJECT TERMS Composites, fiber-reinforced polymers, orthotropic plasticity, orthotropic failure, delamination, computational plasticity				
16. SECURITY CLASSIFICATION OF:			17. LIMITATION OF ABSTRACT None	18. NUMBER OF PAGES 32
a. REPORT Unclassified	b. ABSTRACT Unclassified	c. THIS PAGE Unclassified		
			19a. NAME OF RESPONSIBLE PERSON Timothy Talladay	
			19b. TELEPHONE NUMBER (Include area code) 586-282-0912	

UNCLASSIFIED

Table of Contents

	Page
1.0 Introduction	1
2.0 Orthotropic Model Formulation	3
2.1 Material Reference Frame	3
2.2 Orthotropic Elasticity	4
2.3 Orthotropic Plasticity	5
2.4 Elastic-Plastic Constitutive Update	7
2.5 Orthotropic Damage and Failure	10
3.0 Numerical Examples	13
3.1 Taylor Anvil	13
3.2 Tensile Tests	15
3.3 Ballistic Impacts	17
4.0 Summary and Conclusions	21
5.0 Acknowledgement	23
6.0 References	25

UNCLASSIFIED

List of Figures

	Page
Figure 1. One approach to modeling composites in EPIC: bar elements represent the yarns of fibers and solid elements represent the matrix.....	1
Figure 2. The rotations that transform an element of material between its initial, material, and current orientations.....	4
Figure 3. Depictions of the forward-Euler (left) and backward-Euler (right) finite-difference schemes in time for the elastic-plastic stress update. The six-dimensional stress space is shown in two dimensions, and the yield surface is indicated by the red lines	8
Figure 4. An example of an elastic predictor that lies outside the space (shaded gray) spanned by the plastic correctors in a forward-Euler scheme. In this scenario, the timestep is too large for the rate of loading	10
Figure 5. Plastic strains in a cylinder impacting a rigid surface as viewed from above. Part a is the initial configuration; part b is the response using isotropic material constants in the Hill yield function, and parts c-h are the responses using 50% increases in the individual yield stresses	14
Figure 6. Tensile-test results of composites of S-2 glass fibers and polyester matrix performed by Espinosa <i>et al</i> [5]. The stress-strain curves from the tests are shown in part c, and from EPIC computations in part d	15
Figure 7. Plane-of-symmetry view (top) of the initial configuration of a cylinder impacting a composite target, and the ballistic limits resulting from variations in the individual yield strengths in the composite (bottom)	17

UNCLASSIFIED

List of Tables

	Page
Table 1. Isotropic Material Parameters Used for the Computation of a Cylinder Impacting a Rigid Surface.....	13
Table 2. Orthotropic Model Parameters Used to Simulate the Tensile Tests of Espinosa <i>et al</i> [5].....	16
Table 3. Reference Material Parameters Representing a Balanced Weave Composite, and Used to Compute a Ballistic Limit of 360 m/s When Impacted by a Cylinder 2.4 cm in Diameter.....	18

UNCLASSIFIED

1.0 Introduction

Composites of fiber-reinforced polymers (FRPs) respond to impact loading in a variety of inelastic modes of deformation, depending on such variables as the thickness of the composite section relative to the width of the impactor, the mechanical properties of the fibers and the matrix material, the bonding between the fibers and the matrix, the weave of the fibers, and the impact velocity. In an effort to understand these inelastic modes, much research has recently focused on the mechanics of composites under impact at the meso-scale. This research includes some numerical simulations of composites at the meso-scale, in which the matrix material and yarns of fibers are modeled by separate finite elements. Such simulations shed light on the inelastic modes of interest, but they generally require too much mesh refinement to be useful at the macroscopic scale of design analysis. Therefore, in the analysis of FRP applications, some degree of material homogenization is generally necessary.

Two approaches are now available to model FRP composites in EPIC [1]. In one approach, homogenization is restricted to the individual materials. With this restriction, a uniaxial-stress model for the fibers is implemented in bar elements, while an isotropic elastic-plastic model for the matrix is implemented in 3D solid elements, and the two element types interact through common nodes in the mesh [2]. A sketch of this modeling approach is shown in Figure 1. Homogenization refers to the representation of multiple yarns, including those from multiple plies of fabric, by the same bar element. Similarly, the matrix material separated by plies of fabric is represented by the same solid element. The primary advantage of this approach is that the mechanical properties of the fabric can be acquired from laboratory experiments and applied directly to the bar elements. The primary disadvantage is that the bar elements occupy no volume, the solid elements necessarily occupy one-hundred percent of the composite volume, and the properties of the solid elements therefore cannot be acquired from experiments; they must be extrapolated from the properties of the matrix material.

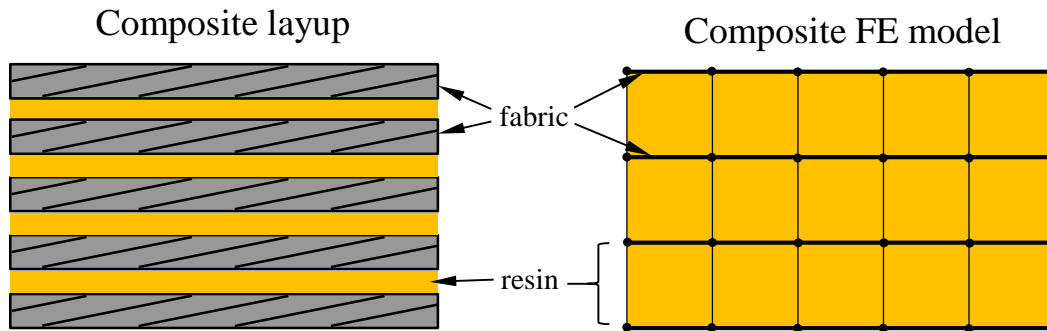


Figure 1. One approach to modeling composites in EPIC: bar elements represent the yarns of fibers and solid elements represent the matrix.

In the second approach to modeling composites in EPIC, the responses of the fibers and the matrix material are homogenized into a single material model, and that model is implemented in 3D solid elements. This approach represents full homogenization of the composite material, and it has been implemented via various anisotropic material models [3-6] in other finite-element codes. The primary advantage of this approach is that the difference between modeling an isotropic metal and an orthotropic composite is confined to the material model, so that mesh generation is identical for all materials. The primary disadvantage is the relative complexity of the material model that is required to adequately represent an orthotropic continuum. This report documents the integration of orthotropic plasticity and failure models into the existing

UNCLASSIFIED

orthotropic elasticity model in EPIC for the purpose of modeling FRP composites under ballistic impact with full material homogenization. It includes a section of example computations to demonstrate the orthotropic models and evaluate how well they apply to FRP composites.

2.0 Orthotropic Model Formulation

Several models have been proposed in the literature for specific fiber-reinforced polymers. In general, these models include assumptions germane to the specific composites of interest, and generate computed results that correlate well with the laboratory tests under consideration. For example, visco-plastic models for glass-fiber composites are typically simplified by only admitting elastic strains in the directions of the fibers [5]. This simplifying assumption is supported by the linearity of the stress-strain curve up to failure in tensile tests along the directions of the fibers, especially in comparison to the non-linear stress-strain curves obtained from off-axis tensile tests.

A somewhat more general approach has been taken for EPIC, based on the desire to treat as many composite materials as practical with one model, but also based on the recognition that the complexities of composite materials make an optimal model difficult to identify before exhaustive tests and computations have been performed. The approach consists of adding orthotropic plasticity and failure models to the existing orthotropic elasticity model in EPIC. This section describes the implementation of those models.

2.1 Material Reference Frame

When finite rotations or large displacements are considered, a finite-element analysis must account for the change in orientation of the material with time. If the material is isotropic, the constitutive models are often cast in rate form, with a suitable stress rate to update the Cauchy stress tensor in the rotating material. But when the material is anisotropic, it also becomes necessary to monitor the orientation of the principal material directions, since they may each exhibit unique behavior. This can be done most naturally by evaluating the constitutive equations in a frame that rotates with the material, i.e., a material reference frame.

The equations of motion must be updated in a global, inertial reference frame. If the constitutive equations are evaluated in the material frame, it becomes necessary to transform between the two frames each timestep. Figure 2 depicts the two reference frames, and the transformations necessary to evaluate the constitutive models in a material reference frame. In the figure, the global frame is represented by X , Y and Z ; and the material frame is represented by X_1 , X_2 and X_3 . The rotation tensor, \mathbf{R} , transforms vectors and tensors from the material frame to the global frame. It is composed of the initial orientation of the global frame with respect to the material frame, $\mathbf{R}_{t=0}$, and the subsequent rotation of the material during the computation, $\mathbf{R}_{t>0}$. The algorithm in EPIC for updating the rotation tensor was first proposed by Dienes [7]. Rather than referring to the initial configuration each timestep, the algorithm updates the rotations using the rates of deformation. Anderson et al [8] discuss the algorithm in detail.

The practice of updating the Cauchy stress tensor of an orthotropic material in the material frame exactly accounts for finite rotations, but does not account for finite shearing deformations. This practice will provide adequate accuracy when shear strains are small, with errors accruing only when non-negligible material strength exists under finite shear strains. A total Lagrangian formulation would account for finite shear strains because the stress update is performed on the Piola-Kirchoff stress tensors, which are cast with respect to the initial unstrained configuration. However, the advantages of such a formulation are not clear, given the current limitations in accuracy of homogenized inelastic models of composites.

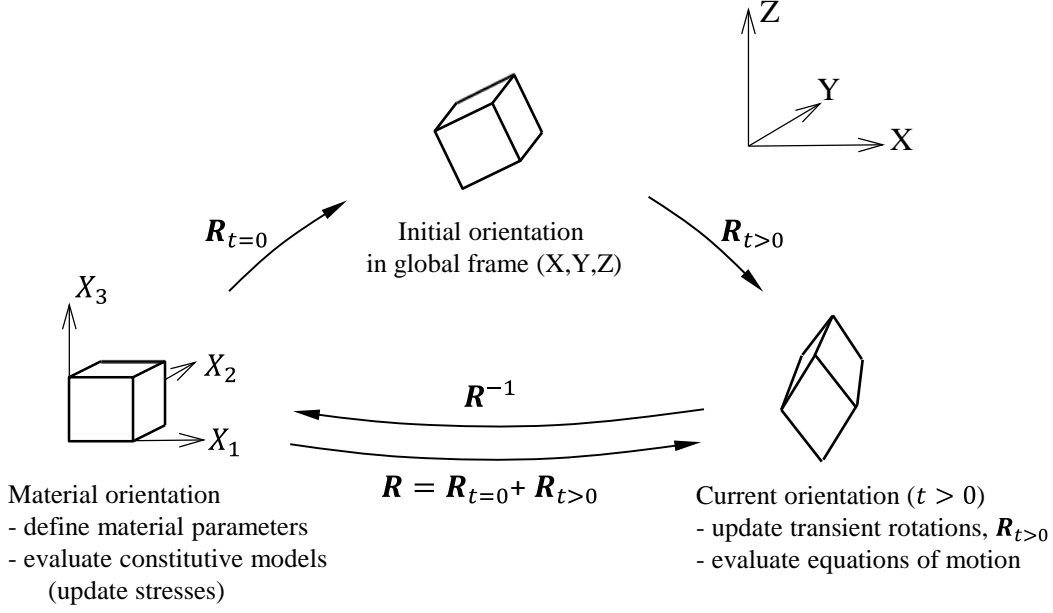


Figure 2. The rotations that transform an element of material between its initial, material, and current orientations.

2.2 Orthotropic Elasticity

The orthotropic elasticity model in EPIC [1] is a generalization of small-strain orthotropic elasticity to finite strains by treating each timestep Δt of the explicit computation as an increment of small strain. As a result, the incremental stress-strain relationship remains linear, and takes the following form.

$$\mathbf{D}^e = \frac{1}{\Delta t} \mathbf{C}^{-1} : \Delta \boldsymbol{\sigma} \quad (1)$$

In this equation, \mathbf{D}^e is the elastic rate-of-deformation tensor that results from an additive decomposition of the rate-of-deformation tensor into elastic and plastic parts, $\mathbf{D} = \mathbf{D}^e + \mathbf{D}^p$; $\Delta \boldsymbol{\sigma}$ is the increment in Cauchy stress; and \mathbf{C} is the tensor of elastic moduli. In EPIC, this equation is implemented via central differences because the velocity gradients of the rate-of-deformation tensor are evaluated at the midsteps. Expressing this incremental elastic relationship in matrix form,

$$\begin{Bmatrix} D_{11}^e \\ D_{22}^e \\ D_{33}^e \\ D_{12}^e \\ D_{13}^e \\ D_{23}^e \end{Bmatrix} = \frac{1}{\Delta t} \begin{bmatrix} \frac{1}{E_1} & -\nu_{21} & -\nu_{31} & 0 & 0 & 0 \\ E_1 & E_2 & E_3 & 0 & 0 & 0 \\ -\nu_{12} & \frac{1}{E_2} & -\nu_{32} & 0 & 0 & 0 \\ E_1 & E_2 & E_3 & 0 & 0 & 0 \\ -\nu_{13} & -\nu_{23} & \frac{1}{E_3} & 0 & 0 & 0 \\ E_1 & E_2 & E_3 & 0 & 0 & 0 \\ 0 & 0 & 0 & \frac{1}{2G_{12}} & 0 & 0 \\ 0 & 0 & 0 & 0 & \frac{1}{2G_{13}} & 0 \\ 0 & 0 & 0 & 0 & 0 & \frac{1}{2G_{23}} \end{bmatrix} \begin{Bmatrix} \Delta \sigma_{11} \\ \Delta \sigma_{22} \\ \Delta \sigma_{33} \\ \Delta \sigma_{12} \\ \Delta \sigma_{13} \\ \Delta \sigma_{23} \end{Bmatrix} \quad (2)$$

In this expression, the three Young's moduli (E_1, E_2, E_3) and the six Poisson's ratios ($\nu_{12}, \nu_{21}, \nu_{13}, \nu_{31}, \nu_{23}, \nu_{32}$) can be obtained from tensile tests in the three principal material directions. But they are not all independent; symmetry considerations impose three conditions on the elastic moduli that reduce the number of independent constants from twelve to nine: $\nu_{21} = \nu_{12}E_2/E_1$, $\nu_{31} = \nu_{13}E_3/E_1$ and $\nu_{32} = \nu_{23}E_3/E_2$.

Because the stresses are updated each timestep from the deformations, the incremental elastic relations must be inverted,

$$\Delta\sigma = \Delta t \mathbf{C} : \mathbf{D}^e \quad (3)$$

Or, in matrix notation,

$$\begin{Bmatrix} \Delta\sigma_{11} \\ \Delta\sigma_{22} \\ \Delta\sigma_{33} \\ \Delta\sigma_{12} \\ \Delta\sigma_{13} \\ \Delta\sigma_{23} \end{Bmatrix} = \Delta t \begin{bmatrix} \frac{1-\nu_{23}\nu_{32}}{E_2E_3\beta} & \frac{\nu_{21}+\nu_{31}\nu_{23}}{E_2E_3\beta} & \frac{\nu_{31}+\nu_{21}\nu_{32}}{E_2E_3\beta} & 0 & 0 & 0 \\ \frac{\nu_{21}+\nu_{31}\nu_{23}}{E_2E_3\beta} & \frac{1-\nu_{13}\nu_{31}}{E_1E_3\beta} & \frac{\nu_{32}+\nu_{12}\nu_{31}}{E_1E_3\beta} & 0 & 0 & 0 \\ \frac{\nu_{31}+\nu_{21}\nu_{32}}{E_2E_3\beta} & \frac{\nu_{32}+\nu_{12}\nu_{31}}{E_1E_3\beta} & \frac{1-\nu_{12}\nu_{21}}{E_1E_2\beta} & 0 & 0 & 0 \\ 0 & 0 & 0 & 2G_{12} & 0 & 0 \\ 0 & 0 & 0 & 0 & 2G_{13} & 0 \\ 0 & 0 & 0 & 0 & 0 & 2G_{23} \end{bmatrix} \begin{Bmatrix} D_{11}^e \\ D_{22}^e \\ D_{33}^e \\ D_{12}^e \\ D_{13}^e \\ D_{23}^e \end{Bmatrix} \quad (4)$$

where $\beta = (1 - \nu_{12}\nu_{21} - \nu_{23}\nu_{32} - \nu_{31}\nu_{13} - 2\nu_{21}\nu_{32}\nu_{13})/(E_1E_2E_3)$.

2.3 Orthotropic Plasticity

The primary limitation on the generality of the plasticity model is the choice of the functional form of the yield surface. The Hill yield surface [9] was originally introduced to model orthotropic metal plasticity. Several other orthotropic yield surfaces have been proposed since then, with the aim to improve accuracy for specific material classes, but no consensus has been reached on the best functional form for FRP composites. As a result, the Hill yield surface has been implemented in EPIC, with the goal of fully evaluating its applicability to FRP composites as test data become available. This yield surface is quadratic in the stress components,

$$f(\sigma) = \frac{1}{2} [F(\sigma_{22} - \sigma_{33})^2 + G(\sigma_{33} - \sigma_{11})^2 + H(\sigma_{11} - \sigma_{22})^2] + N\sigma_{12}^2 + M\sigma_{13}^2 + L\sigma_{23}^2 - \sigma^2 = 0 \quad (5)$$

In this equation, the subscripts on the stresses refer to the orthogonal principal directions of the material. For a fiber composite composed of 0/90-degree plies, two of the principal directions align with the fiber directions, and the third principal direction is normal to the plane of the composite.

The model parameters are F, G, H, N, M and L ; and the average radius of the yield surface in stress space is represented by σ . The normal yield stresses ($\sigma_{11}^y, \sigma_{22}^y$, and σ_{33}^y) and shear yield stresses ($\sigma_{12}^y, \sigma_{13}^y$, and σ_{23}^y) are aligned with the principal material directions, and they are used to determine the model parameters:

$$F = \left(\frac{\sigma}{\sigma_{22}^y}\right)^2 + \left(\frac{\sigma}{\sigma_{33}^y}\right)^2 - \left(\frac{\sigma}{\sigma_{11}^y}\right)^2 \quad (6)$$

$$G = \left(\frac{\sigma}{\sigma_{33}^y}\right)^2 + \left(\frac{\sigma}{\sigma_{11}^y}\right)^2 - \left(\frac{\sigma}{\sigma_{22}^y}\right)^2 \quad (7)$$

$$H = \left(\frac{\sigma}{\sigma_{11}^y}\right)^2 + \left(\frac{\sigma}{\sigma_{22}^y}\right)^2 - \left(\frac{\sigma}{\sigma_{33}^y}\right)^2 \quad (8)$$

$$N = \left(\frac{\sigma}{\sigma_{12}^y}\right)^2 \quad (9)$$

$$M = \left(\frac{\sigma}{\sigma_{13}^y}\right)^2 \quad (10)$$

$$L = \left(\frac{\sigma}{\sigma_{23}^y}\right)^2 \quad (11)$$

The yield stresses are the inputs to EPIC that define the Hill yield surface, and the model parameters are computed from the yield stresses according to equations 6-11.

Material hardening with inelastic strains has been implemented through the average normal radius of the yield surface, σ .

$$\sigma = \frac{1}{3}(\sigma_{11}^y + \sigma_{22}^y + \sigma_{33}^y)(1 + C_1 \varepsilon_p^{C_2}) \quad (12)$$

In this equation, the initial average yield stress is factored by the hardening term, $(1 + C_1 \varepsilon_p^{C_2})$, ε_p is the effective plastic strain, and C_1 and C_2 are the hardening parameters. Since ε_p is a scalar, hardening is isotropic, i.e., it does not depend upon the orientation of the inelastic strains. Hardening in this form can be interpreted as a uniform scaling of the yield surface in all directions of stress space.

To complete a model of inelastic deformations, the inelastic strains must be characterized by a flow rule. An associated flow rule enforces the principal of normality, associating the direction of inelastic rates of deformation with the normal to the yield surface. While some frictional materials do not obey the principal of normality, most others do. As a result, an associated flow rule has been chosen for the orthotropic inelastic model in EPIC,

$$\mathbf{D}^p = \lambda \frac{\partial f}{\partial \boldsymbol{\sigma}} \quad (13)$$

In this equation, \mathbf{D}^p is the plastic rate-of-deformation tensor; $\frac{\partial f}{\partial \boldsymbol{\sigma}}$ is the normal to the yield surface f , and the scalar λ is the plastic proportionality factor. When the yield surface is quadratic in the stress components, like the Hill yield surface, the normal to the surface is linear in the stress components, and the associated flow rule takes the following form,

$$\mathbf{D}^p = \lambda \mathbf{L} : \boldsymbol{\sigma} \quad (14)$$

In this equation, \mathbf{L} is a tensor of constant coefficients. In matrix notation,

$$\begin{Bmatrix} D_{11}^p \\ D_{22}^p \\ D_{33}^p \\ D_{12}^p \\ D_{13}^p \\ D_{23}^p \end{Bmatrix} = \lambda \begin{bmatrix} G+H & -H & -G & 0 & 0 & 0 \\ -H & H+F & -F & 0 & 0 & 0 \\ -G & -F & F+G & 0 & 0 & 0 \\ 0 & 0 & 0 & N & 0 & 0 \\ 0 & 0 & 0 & 0 & M & 0 \\ 0 & 0 & 0 & 0 & 0 & L \end{bmatrix} \begin{Bmatrix} \sigma_{11} \\ \sigma_{22} \\ \sigma_{33} \\ \sigma_{12} \\ \sigma_{13} \\ \sigma_{23} \end{Bmatrix} \quad (15)$$

2.4 Elastic-Plastic Constitutive Update

The incremental elastic-plastic constitutive update is expressed by substituting $\mathbf{D}^e = \mathbf{D} - \mathbf{D}^p$ into the incremental elastic update of equation 3,

$$\Delta \boldsymbol{\sigma} = \Delta t \mathbf{C} : (\mathbf{D} - \mathbf{D}^p) \quad (16)$$

Further substitution of the flow rule in equation 14 for \mathbf{D}^p yields,

$$\Delta \boldsymbol{\sigma} = \Delta t \mathbf{C} : (\mathbf{D} - \lambda \mathbf{L} : \boldsymbol{\sigma}) \quad (17)$$

The stress increment is then expressed explicitly as $\Delta \boldsymbol{\sigma} = \boldsymbol{\sigma}_{n+1} - \boldsymbol{\sigma}_n$, in which $\boldsymbol{\sigma}_n$ and $\boldsymbol{\sigma}_{n+1}$ are the stress tensors at the beginning and end of the $(n+1)$ th timestep, respectively. Also, the variable ξ is substituted for the product $\lambda \Delta t$.

$$\boldsymbol{\sigma}_{n+1} = \boldsymbol{\sigma}_n + \Delta t \mathbf{C} : \mathbf{D} - \xi \mathbf{C} : \mathbf{L} : \boldsymbol{\sigma} \quad (18)$$

Finally, rearranging terms gives,

$$\boldsymbol{\sigma}_n + \Delta t \mathbf{C} : \mathbf{D} = \boldsymbol{\sigma}_{n+1} + \xi \mathbf{C} : \mathbf{L} : \boldsymbol{\sigma} \quad (19)$$

The two terms on the left side of equation 19 are known at the beginning of the elastic-plastic constitutive update, and are referred to collectively as the elastic predictor of the updated stress, $\boldsymbol{\sigma}^* = \boldsymbol{\sigma}_n + \Delta t \mathbf{C} : \mathbf{D}$. The first term on the right side is the desired solution for the updated stress, and it is limited by the yield surface. The second term on the right side, $\xi \mathbf{C} : \mathbf{L} : \boldsymbol{\sigma}$, is the plastic corrector, since it represents the difference between the elastic predictor and the updated stress. The plastic corrector is linear in the stress, with constant coefficients \mathbf{C} and \mathbf{L} , and the unknown scalar coefficient ξ .

If the elastic predictor lies within the yield surface, $(\boldsymbol{\sigma}_n + \Delta t \mathbf{C} : \mathbf{D}) - \sigma^2 \leq 0$, then the rate of deformation is entirely elastic for that timestep, the plastic corrector is zero, and the updated stress is set equal to the elastic predictor. If the elastic predictor exceeds the yield surface, then the plastic corrector is nonzero and the expression for $\boldsymbol{\sigma}_{n+1}$ must be solved simultaneously with $f(\boldsymbol{\sigma}_{n+1}) - \sigma^2 = 0$.

The method of this solution depends upon the choice of $\boldsymbol{\sigma}$ in the plastic corrector. To maintain consistency with the governing differential equation, $\boldsymbol{\sigma}$ must be on the interval from $\boldsymbol{\sigma}_n$ to $\boldsymbol{\sigma}_{n+1}$. Two schemes of first-order accuracy are obtained if $\boldsymbol{\sigma}$ is assigned its values at the endpoints of the timestep. If the value is at the beginning of the timestep, $\boldsymbol{\sigma} = \boldsymbol{\sigma}_n$, then the normal to the yield surface during the timestep is approximated by its value at the beginning of the timestep, i.e., $\frac{\partial f}{\partial \boldsymbol{\sigma}} \approx \lambda \mathbf{L} : \boldsymbol{\sigma}_n$, the plastic corrector becomes $\xi \mathbf{C} : \mathbf{L} : \boldsymbol{\sigma}_n$, and the resulting finite-difference scheme is referred to as a forward-Euler scheme. If, on the other hand, the value is at the end of the timestep, $\boldsymbol{\sigma} = \boldsymbol{\sigma}_{n+1}$, then the normal to the yield surface is approximated by its

value at the end of the timestep, $\frac{\partial f}{\partial \sigma} \approx \lambda \mathbf{L} : \boldsymbol{\sigma}_{n+1}$, the plastic corrector becomes $\xi \mathbf{C} : \mathbf{L} : \boldsymbol{\sigma}_{n+1}$, and the resulting scheme is referred to as a backward-Euler scheme. In developing an option for orthotropic elasto-plasticity in EPIC, both of these schemes have been implemented. The remainder of this section describes the implementations of these schemes, while the following section on numerical examples includes a comparison of their performances.

Figure 3 depicts the solution procedure in stress space for both finite-difference schemes. (Due to graphical limitations, the six-dimensional stress space is reduced to two dimensions.) The yield surface is represented by the red line, and denoted by $f(\boldsymbol{\sigma}) - \sigma^2 = 0$. The state of stress at the beginning of the timestep, $\boldsymbol{\sigma}_n$, is located inside the yield surface, while the elastic predictor, $\boldsymbol{\sigma}^*$, is outside the yield surface. This represents the most general case of an elasto-plastic stress update.

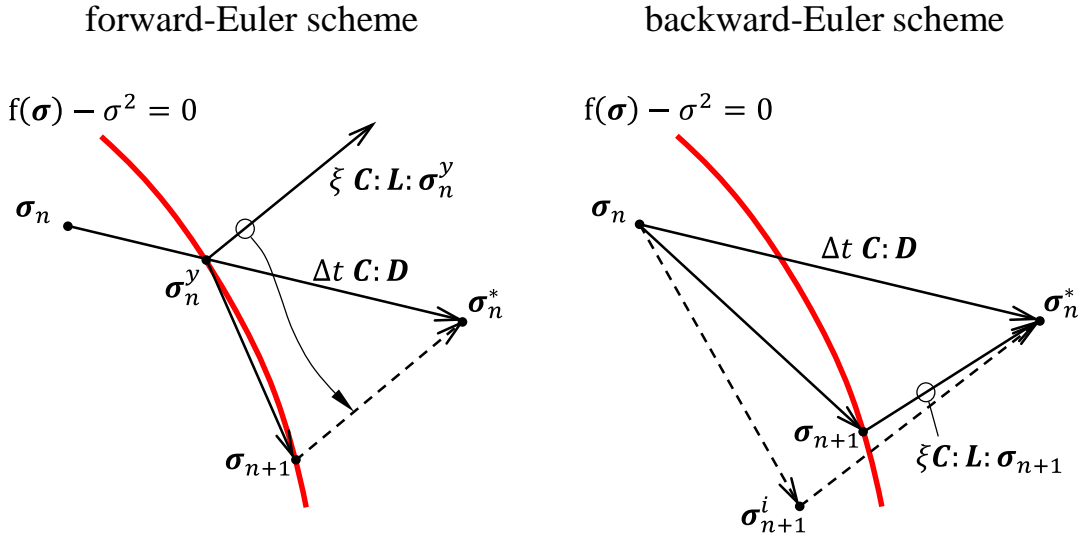


Figure 3. Depictions of the forward-Euler (left) and backward-Euler (right) finite-difference schemes in time for the elastic-plastic stress update. The six-dimensional stress space is shown in two dimensions, and the yield surface is indicated by the red lines.

On the left side of the figure is the forward-Euler scheme. In this scheme, it is first necessary to find the stress state along the path of the elastic predictor that lies on the yield surface. This stress state is denoted by $\boldsymbol{\sigma}_n^y$, and it is interpolated between the known stress states $\boldsymbol{\sigma}_n$ and $\boldsymbol{\sigma}^*$ as $\boldsymbol{\sigma}_n^y = (1 - \alpha) \boldsymbol{\sigma}_n + \alpha \boldsymbol{\sigma}^*$. It is determined by solving for α in the yield condition,

$$f(\boldsymbol{\sigma}_n^y) - \sigma^2 = f((1 - \alpha) \boldsymbol{\sigma}_n + \alpha \boldsymbol{\sigma}^*) - \sigma^2 = 0 \quad (20)$$

Since the yield surface is quadratic in the stresses, which are in turn linear in the unknown α , this expression reduces to a quadratic equation in α , and can therefore be solved explicitly. The direction of the plastic corrector is then calculated from $\boldsymbol{\sigma}_n^y$ as $\xi \mathbf{C} : \mathbf{L} : \boldsymbol{\sigma}_n^y$, and it is represented in the figure by the solid arrow emanating from $\boldsymbol{\sigma}_n^y$. The expression for the updated stress is then substituted into the equation of the yield surface,

$$f(\boldsymbol{\sigma}_{n+1}) - \sigma^2 = f(\boldsymbol{\sigma}^* - \xi \mathbf{C} : \mathbf{L} : \boldsymbol{\sigma}_i^y) - \sigma^2 = 0 \quad (21)$$

And this equation is then solved for the unknown scaling factor, ξ , which in turn provides the updated stress state, $\boldsymbol{\sigma}_{n+1}$. The expression for ξ also reduces to a quadratic equation, with an

explicit solution. Therefore, the forward-Euler scheme for the elasto-plastic stress update is explicit, and its graphical representation is the connection of stress states $\boldsymbol{\sigma}^*$ and $\boldsymbol{\sigma}_{n+1}$ by the dashed arrow on the left side of Fig 3.

The right side of Fig. 3 depicts the backward-Euler scheme. In this scheme, the direction of the plastic corrector, $\xi \mathbf{C} : \mathbf{L} : \boldsymbol{\sigma}_{n+1}$, depends on the unknown updated stress, $\boldsymbol{\sigma}_{n+1}$, which lies on the yield surface. There is therefore no need to find the stress state along the path of the elastic predictor that lies on the yield surface. Substituting $\boldsymbol{\sigma}_{n+1}$ for $\boldsymbol{\sigma}$ in the elasto-plastic stress update yields,

$$\boldsymbol{\sigma}_n + \Delta t \mathbf{C} : \mathbf{D} = (\mathbf{I} + \xi \mathbf{C} : \mathbf{L}) : \boldsymbol{\sigma}_{n+1} \quad (22)$$

where \mathbf{I} is the fourth-order identity tensor. Substituting $\boldsymbol{\sigma}^*$ for the elastic predictor on the left side of equation 22, and solving for the updated stress,

$$\boldsymbol{\sigma}_{n+1} = (\mathbf{I} + \xi \mathbf{C} : \mathbf{L})^{-1} : \boldsymbol{\sigma}^* \quad (23)$$

Due to the symmetry of the stress tensor, this expression represents a system of six equations. They express the unknown stresses $\boldsymbol{\sigma}_{n+1}$ as rational algebraic functions of the unknown scalar ξ , and they must be solved simultaneously with the yield condition $f(\boldsymbol{\sigma}_{n+1}) - \sigma^2 = 0$. Analytic expressions for the inverse of $(\mathbf{I} + \xi \mathbf{C} : \mathbf{L})$ have been derived for EPIC, and a Newton-Raphson iterative method on the yield condition has been implemented for the solution of the updated stresses.

The Newton-Raphson method begins with an estimate of ξ . An iterative loop is then entered in which an estimate of the updated stress is computed from ξ using the inverse of $(\mathbf{I} + \xi \mathbf{C} : \mathbf{L})$. On the right side of Fig. 3, this estimated stress state is denoted by $\boldsymbol{\sigma}_{n+1}^i$, where the superscript i indicates the iteration count. Since this stress state has been computed from an estimate of ξ , $\boldsymbol{\sigma}_{n+1}^i$ does not lie on the yield surface in the figure. The yield condition, $(\boldsymbol{\sigma}_{n+1}^i) - \sigma^2$, and its derivative with respect to ξ , $\frac{\partial f(\boldsymbol{\sigma}_{n+1}^i)}{\partial \xi} = \frac{\partial f}{\partial \boldsymbol{\sigma}} \cdot \frac{\partial \boldsymbol{\sigma}}{\partial \xi}$, are then computed and the estimate of ξ is improved via the Newton-Raphson method. The approximate solution to the updated stress, $\boldsymbol{\sigma}_{n+1}^i$, approaches the yield surface with each successive iteration on the value of $f(\boldsymbol{\sigma}_{n+1}^i) - \sigma^2$, until the desired tolerance on the root of this expression has been met. The final value of $\boldsymbol{\sigma}_{n+1}^i$ is then assigned to $\boldsymbol{\sigma}_{n+1}$, and the algorithm exits the iterative loop.

The quality of the initial estimate of ξ affects both the reliability and efficiency of the iterative method. The reliability is reflected by the rate of success in finding the solution, and the efficiency is reflected by the number of iterations required. An initial estimate of ξ that has proven very reliable and efficient is obtained by scaling the elastic predictor back to the yield surface along the line to the origin of stress space, computing the direction of the plastic corrector at that stress state, and projecting $\boldsymbol{\sigma}^* - \boldsymbol{\sigma}_n$ onto that direction.

When plasticity is coupled with orthotropic elasticity, the tensor of elastic constants generally rotates the plastic corrector away from the normal to the yield surface, $\lambda \mathbf{C} : \frac{\partial f}{\partial \boldsymbol{\sigma}}$, as depicted for both schemes in Fig. 3. In the special case of isotropic elasticity, the elasto-plastic stress update can be expressed in terms of the deviatoric stress, the tensor of elastic constants

reduces to a scalar multiple of the identity tensor, $\mathbf{C} = 2G\mathbf{I}$, and the plastic corrector is therefore normal to the yield surface.

Although the forward and backward Euler schemes are both first-order accurate, a significant practical difference exists between the two methods, and it results from representing the normal to the yield surface by its value either at the beginning or end of the timestep. If the normal to the yield surface is represented by its value at the end of the timestep, as in the backward Euler scheme, then the direction of the plastic corrector varies with the solution, $\boldsymbol{\sigma}_{n+1}$. Given a smooth yield surface, this variation in the directions of the plastic correctors allows them to span the entire space of elastic predictors, guaranteeing a solution to the backward Euler scheme.

If the normal to the yield surface is represented by its value at the beginning of the timestep, as in the forward-Euler scheme, then the direction of the plastic corrector is fixed for all points on the yield surface, and the plastic correctors span only a subset of the space of elastic predictors. An elastic predictor that lies outside the space of forward-Euler plastic correctors is depicted in Fig. 4. Here, the fixed direction of the plastic corrector has been copied to several locations along the yield surface, as indicated by the dashed arrows, and the resulting space spanned by the plastic correctors is shaded gray. This figure demonstrates the loss of a solution to the forward-Euler scheme that may occur when the timestep is too large for the rate of loading.

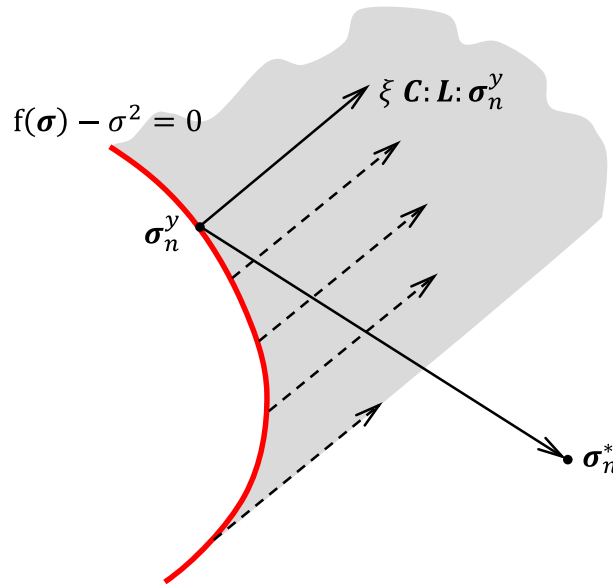


Figure 4. An example of an elastic predictor that lies outside the space (shaded gray) spanned by the plastic correctors in a forward-Euler scheme. In this scenario, the timestep is too large for the rate of loading.

The Hill yield function reduces to the von Mises yield function when $F = G = H = 1$ and $N = M = L = 3$. When the von Mises yield function is implemented with isotropic elasticity, the initial estimate of ξ in the backward-Euler scheme provides the converged solution, and the scheme reduces to the familiar radial-return algorithm.

2.5 Orthotropic Damage and Failure

To complete an orthotropic material model for the ballistic impact of composites, an orthotropic failure model has also been implemented in EPIC. This model acts in conjunction

with the orthotropic elasticity and plasticity models described in the preceding sections. It compiles components of the plastic natural-strain tensor associated with the principal material directions, and fails the material by eliminating the deviatoric stresses when any of the plastic strain components reaches its user-supplied critical value.

The plastic natural-strain tensor can be derived from the rate-of-deformation tensor, beginning with the relation (Malvern, [11]) between the rate-of-deformation tensor \mathbf{D} and the infinitesimal line segment $d\mathbf{x}$,

$$\frac{d}{dt}(ds^2) = 2 d\mathbf{x} \cdot \mathbf{D} \cdot d\mathbf{x} \quad (24)$$

In this expression, ds is the magnitude of the line segment, $d\mathbf{x} = ds \mathbf{n}$, where \mathbf{n} is a unit vector in the direction of $d\mathbf{x}$. This expression indicates that the rate-of-deformation tensor measures the instantaneous rate of change of the squared length of an infinitesimal line segment. Since ds is associated with the *spatial* segment $d\mathbf{x}$, not the *material* segment $d\mathbf{X}$, integration of this expression in time with respect to an inertial reference frame does not generally produce a material metric. In this implementation, however, the reference frame is the material frame, which moves and rotates with the material, and temporal integration is meaningful in the small-strain limit. Therefore, replacing the differentials by finite differences between t_n and t_{n+1} ,

$$(ds_{n+1})^2 - (ds_n)^2 = 2 \Delta t d\mathbf{x} \cdot \mathbf{D} \cdot d\mathbf{x} \quad (25)$$

And factoring the left side,

$$(ds_{n+1} + ds_n)(ds_{n+1} - ds_n) = 2 \Delta t d\mathbf{x} \cdot \mathbf{D} \cdot d\mathbf{x} \quad (26)$$

Denoting the mid-step segment magnitude as $ds_{n+1/2} = (ds_{n+1} + ds_n)/2$ and dividing by twice its square,

$$(ds_{n+1} - ds_n)/ds_{n+1/2} = \Delta t \frac{d\mathbf{x}}{ds_{n+1/2}} \cdot \mathbf{D} \cdot \frac{d\mathbf{x}}{ds_{n+1/2}} \quad (27)$$

For the increment in time from t_n to t_{n+1} , the two fractions on the right side are the unit vector, \mathbf{n} , and the left side is an increment in natural strain $\Delta\varepsilon$ along $d\mathbf{x}$.

$$\Delta\varepsilon = \Delta t \mathbf{n} \cdot \mathbf{D} \cdot \mathbf{n} \quad (28)$$

From the previous section, the rate-of-deformation tensor is composed of elastic and plastic parts, $\mathbf{D} = \mathbf{D}^e + \mathbf{D}^p$. Similarly, the natural-strain increments can be decomposed into elastic and plastic parts. Substituting these decompositions into equation 28,

$$\Delta\varepsilon^e + \Delta\varepsilon^p = \Delta t \mathbf{n} \cdot (\mathbf{D}^e + \mathbf{D}^p) \cdot \mathbf{n} \quad (29)$$

When the deformation is entirely elastic, equation 29 must reduce to $\Delta\varepsilon^e = \Delta t \mathbf{n} \cdot \mathbf{D}^e \cdot \mathbf{n}$. Subtraction of this expression for $\Delta\varepsilon^e$ from equation 29 gives,

$$\Delta\varepsilon^p = \Delta t \mathbf{n} \cdot \mathbf{D}^p \cdot \mathbf{n} \quad (30)$$

This expression defines the plastic natural-strain tensor in material coordinates.

UNCLASSIFIED

3.0 Numerical Examples

3.1 Taylor Anvil

Computations of a cylinder impacting a rigid surface demonstrate the effects of the orthotropic-plasticity model parameters. They also provide some verification of the model's implementation in EPIC.

The top left corner of Fig. 5 shows an overhead view of the cylinder's mesh in the initial configuration, with the principal material directions superimposed. The mesh is composed of 40,320 tetrahedral elements. The cylinder is 3.0 cm in length and 1.5 cm in diameter, and its impact velocity is 150 m/s. The top right corner of the figure shows the results of the computation using the isotropic model parameters listed in Table 1. The results are colored by effective plastic strain at 100 μ s after impact, when plastic deformation is complete. The results of the isotropic computation are identical to those obtained by using EPIC's model for metal plasticity, which employs the von Mises yield surface and the Johnson-Cook strength model. The isotropic computation therefore verifies that the orthotropic model is correctly implemented in the special case of material isotropy.

Table 1. Isotropic Material Parameters Used for the Computation of a Cylinder Impacting a Rigid Surface

$\rho = 7900 \text{ kg/m}^3$ $E_1 = E_2 = E_3 = 192 \text{ GPa}$ $G_{12} = G_{13} = G_{23} = 80 \text{ GPa}$ $\nu_{12} = \nu_{13} = \nu_{23} = 0.2$ $\sigma_{11}^y = \sigma_{22}^y = \sigma_{33}^y = 175 \text{ MPa}$ $\sigma_{12}^y = \sigma_{13}^y = \sigma_{23}^y = 101 \text{ MPa}$ $C_1 = 0, C_2 = 1$ $\varepsilon_{11}^{pf} = \varepsilon_{22}^{pf} = \varepsilon_{33}^{pf} = \varepsilon_{12}^{pf} = \varepsilon_{13}^{pf} = \varepsilon_{23}^{pf} = 1$
--

By comparison with the orthotropic computations, the isotropic computation also helps to determine the effects of orthotropy. The remaining six plots in Fig. 5 show the results of the orthotropic computations, each with the same material parameters as the isotropic computation, except a 50 percent increase in one of the yield stresses: σ_{11}^y , σ_{22}^y , σ_{33}^y , σ_{12}^y , σ_{13}^y or σ_{23}^y . Parts c, d and e show the plastic strains due to increases in the normal yield strengths, and parts f, g and h show the plastic strains due to increases in the shear yield strengths. When the in-plane normal strengths are increased (parts c and d), or the out-of-plane shear strengths are increased (parts g and h), the deformation of the cylinder is reduced in the respective direction.

These computations were performed with both the forward-Euler and backward-Euler schemes described in the preceding section. To maintain stability, the forward-Euler scheme required a timestep about one tenth that of the Courant condition in the initial configuration, and about one third that of the Courant condition in the final configuration. In contrast, the backward-Euler scheme is stable at the Courant condition. As a result, the run times using the forward-Euler scheme were about five times as long as those using the backward-Euler scheme, as the efficiency gains of the explicit forward-Euler scheme were dwarfed by the inefficiency of the smaller timesteps. The computations in the following two sections were performed with the backward-Euler scheme only.

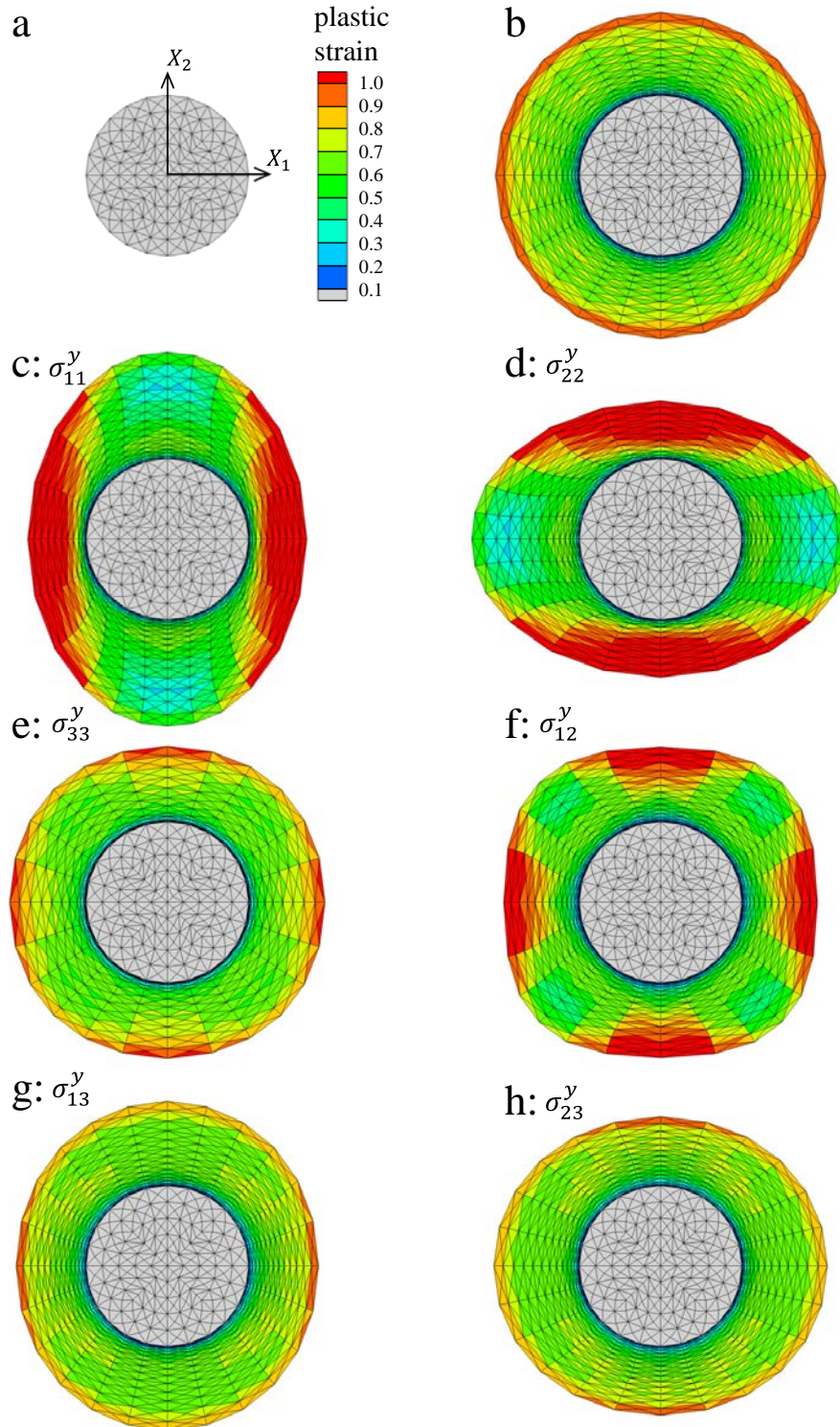


Figure 5. Plastic strains in a cylinder impacting a rigid surface as viewed from above. Part a is the initial configuration; part b is the response using isotropic material constants in the Hill yield function; and parts c-h are the responses using 50% increases in the indicated individual yield stresses.

3.2 Tensile Tests

The mechanical response of a tensile specimen of FRP composite depends strongly on the orientation of the load with respect to the principal material directions. When the direction of the load is aligned with one of the in-plane principal directions, the fiber characteristics dominate the response, and the specimen's stress-strain curve is similar to that of the fibers. However, when the direction of the load bisects the two in-plane principal directions, the fibers allow much larger strains before specimen failure, the matrix material contributes to the response, and the stress-strain curve becomes much softer and more nonlinear.

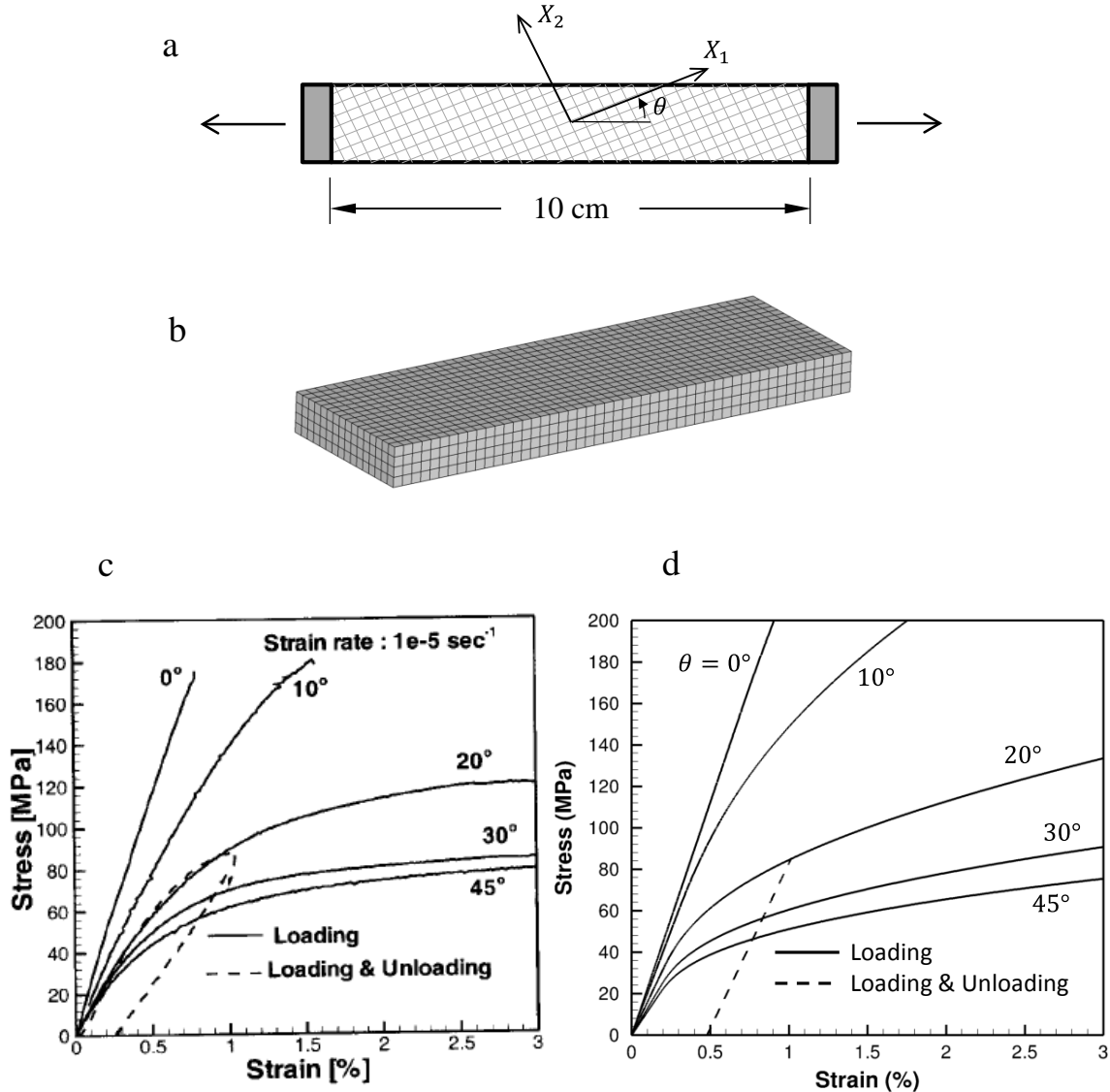


Figure 6. Tensile-test results of composites of S-2 glass fibers and polyester matrix performed by Espinosa *et al* [5]. The stress-strain curves from the tests are shown in part c, and from EPIC computations in part d.

Espinosa *et al* [5] performed tensile tests on composites of woven S-2 glass fibers in a polyester matrix. Part a of Fig. 6 is a diagram of their tensile specimen. Cut from a panel, it is 10 cm long, 1.6 cm wide, and 0.4 cm thick. Loading is applied through strain-compatible fiberglass end tabs. The angle θ is defined by the orientation of the nearest in-plane principal material direction with respect to the loading direction. Specimens loaded along the fibers are therefore designated by $\theta = 0^\circ$. EPIC computations were performed for the same values of θ that were reported by Espinosa *et al*: $\theta = 0^\circ, 10^\circ, 20^\circ, 30^\circ, 45^\circ$. Part b of the figure shows the mesh of 3200 hexahedral elements that represents half of the length of the tensile specimen. A plane of symmetry was enforced at one end of the mesh, and velocities were applied at the other end.

The stress-strain curves reported by Espinosa *et al* are reproduced in Part c of Fig. 6. With increasing θ , the curves demonstrate a decrease in stiffness and large increases in both the nonlinearity of the response and the strains to failure. The material-model parameters listed in Table 2 were used in the EPIC computations, with anisotropy in both the elasticity and plasticity models. These constants were chosen to produce the stress-strain curves shown in part d of Fig. 6. The similarity of the stress-strain curves in parts c and d therefore does not serve as independent validation of the model constants, but rather as a demonstration of the orthotropic model's ability to simulate some of the fundamental characteristics of FRP composites. These characteristics include a nearly linear response to failure when loading along a principal in-plane material direction, and much greater plastic strains as the loading direction deviates from the principal in-plane material direction.

Table 2. Orthotropic Model Parameters Used to Simulate the Tensile Tests of Espinosa *et al* [5]

$\rho = 1800 \text{ kg/m}^3$
$E_1 = E_2 = 22.5 \text{ GPa}$
$E_3 = 15 \text{ GPa}$
$G_{12} = G_{13} = G_{23} = 3.5 \text{ GPa}$
$\nu_{12} = \nu_{13} = \nu_{23} = 0.2$
$\sigma_{11}^y = \sigma_{22}^y = \sigma_{33}^y = 150 \text{ MPa}$
$\sigma_{12}^y = \sigma_{13}^y = \sigma_{23}^y = 10 \text{ MPa}$
$C_1 = 11, C_2 = 0.4$
$\varepsilon_{11}^{pf} = \varepsilon_{22}^{pf} = \varepsilon_{33}^{pf} = 0.005$
$\varepsilon_{12}^{pf} = \varepsilon_{13}^{pf} = \varepsilon_{23}^{pf} = 1$

It should be noted that the experimental results in part c of Fig. 6 indicate failure of the FRP composite at approximately the same load when $\theta = 0^\circ$ and $\theta = 10^\circ$, but at nearly twice the strain when $\theta = 10^\circ$. This behavior suggests that the failure is stress dependent, in contrast to the plastic-strain-dependent failure that has been implemented in the orthotropic model. Further examination of the failure characteristics of FRP composites may therefore be necessary to refine the orthotropic failure model for composites.

Unloading curves with $\theta = 20^\circ$ are represented by dashed lines in parts c and d of Fig. 6. The straight-line path of the computation reflects linear elasticity, while the curved path of the experiment indicates some nonlinearity in the elasticity. Since the stress-strain curves with $\theta = 0^\circ$ are linear, it appears that the strong experimental nonlinearities that occur when $\theta > 0^\circ$ are partially elastic, and that the nonlinear elasticity is due to the polyester matrix.

3.3 Ballistic Impacts

The computations in this section demonstrate the use of the orthotropic model to evaluate FRP composites under ballistic impact. The top of Fig. 7 shows the plane of symmetry of the impact configuration. The square target is 24 cm wide and 1.6 cm thick. It is composed of a composite material, with the first and second principal material directions in the plane of the target, as indicated by the material axes at the top of the figure. The cylindrical projectile is 2.4 cm in diameter and 4.8 cm long, and it is modeled as an isotropic elastic-plastic tool steel [12].

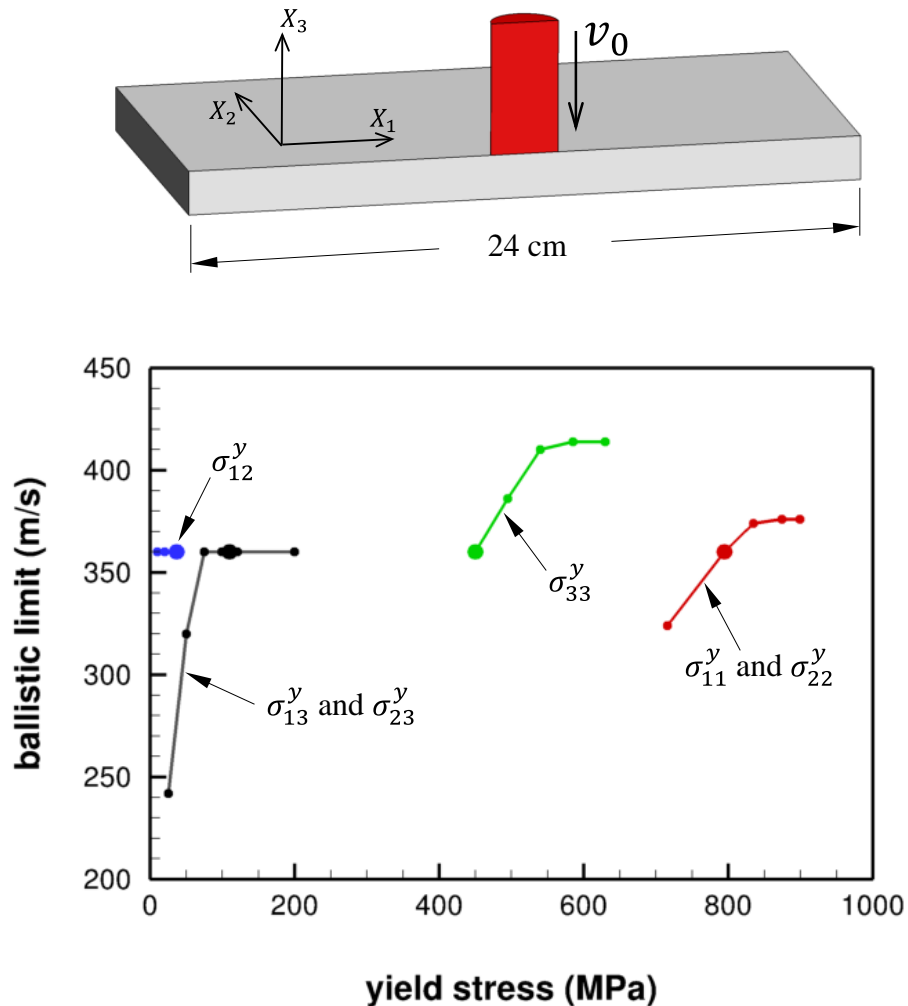


Figure 7. Plane-of-symmetry view (top) of the initial configuration of a cylinder impacting a composite target, and the ballistic limits resulting from variations in the individual yield strengths in the composite (bottom).

Table 3 lists the reference orthotropic material parameters used in the target. Although they do not represent a specific composite material, they include two features of balanced-weave FRPs: equal yield stresses and stiffnesses in the in-plane principal directions, and equal yield stresses and stiffnesses in the transverse shear directions. They also include a transverse normal yield stress, σ_{33}^y , that is significantly less than the in-plane values.

Table 3. Reference Material Parameters Representing a Balanced-Weave Composite, and Used to Compute a Ballistic Limit of 360 m/s When Impacted by a Cylinder 2.4 cm in Diameter

$$\begin{aligned}
 \rho &= 1800 \text{ kg/m}^3 \\
 E_1 &= E_2 = 26 \text{ GPa}, E_3 = 3 \text{ GPa} \\
 G_{12} &= 2.9 \text{ GPa}, G_{13} = G_{23} = 11.3 \text{ GPa} \\
 \nu_{12} &= 0.1, \nu_{13} = \nu_{23} = 0.49 \\
 \sigma_{11}^y &= \sigma_{22}^y = 795 \text{ MPa}, \sigma_{33}^y = 450 \text{ MPa} \\
 \sigma_{12}^y &= 37 \text{ MPa}, \sigma_{13}^y = \sigma_{23}^y = 110 \text{ MPa} \\
 C_1 &= 11, C_2 = 0.4 \\
 \varepsilon_{11}^{pf} &= \varepsilon_{22}^{pf} = 0.02, \varepsilon_{33}^{pf} = 0.2 \\
 \varepsilon_{12}^{pf} &= 0.15, \varepsilon_{13}^{pf} = \varepsilon_{23}^{pf} = 0.3
 \end{aligned}$$

The computations were performed with an erosion strain of 1.5, so that elements on the contact interfaces are removed from the computation when their effective plastic strains reach 150%, and the timestep does not become prohibitively small. Given the critical plastic strains in Table 3, the erosion strain of 1.5 ensures that elements will only be discarded after they have lost strength.

With the reference parameters in Table 3, a ballistic limit of 360 m/s was computed. To evaluate the influence of the yield stresses, ballistic limits were also computed using the reference parameters with variations in the individual yield stresses. Variations of the in-plane normal yield stresses, σ_{11}^y and σ_{22}^y , were coupled, as were variations in the out-of-plane shear yield stresses, σ_{13}^y and σ_{23}^y . For every combination of material parameters, computations were performed at 4 m/s intervals to determine the ballistic limit.

The plot of ballistic limits as a function of the yield stresses at the bottom of Fig. 7 summarizes the results of the computations. The data points from variations in the same yield stress are connected by a line. One data point in each of these sets represents the reference material parameters, and it is indicated by a larger circle than the other data points. The four large circles in the figure therefore represent the ballistic limit (360 m/s) from the same parameters, while the smaller circles each represent the ballistic limit from a unique combination of parameters, with a variation from the reference parameters in one of the yield stresses.

As a yield stress increases, the ballistic limit either increases or remains constant. When the ballistic limit increases, the yield stress is limiting the ballistic performance of the target. And when the ballistic limit remains constant, a different yield stress is limiting the ballistic performance. In the case of these reference parameters, it appears that the normal yield stresses are limiting the ballistic performance, but the shear yield stresses are not. In addition, it appears that the in-plane shear yield stress, σ_{12}^y , will never limit the ballistic performance. Given the very low values of σ_{12}^y for which the ballistic limit has been computed, this observation may apply to many impact configurations and many FRPs. It is also consistent with the good performance of ballistic fabrics, for which σ_{12}^y is essentially zero.

When the reference parameters are changed, or the ratio of target thickness to projectile diameter is increased, the limiting yield stresses will likely change. In particular, the transverse shear yield stresses are expected to limit a thicker target's performance, since tests indicate that delamination becomes a critical mode of inelastic deformation in FRP targets subjected to ballistic impacts.

As mentioned previously, the quadratic form of the Hill yield surface is not sufficiently general to admit any combination of normal yield stresses. Walker and Thacker [13] noted that for orthotropic plates the out-of-plane normal yield stress must be greater than half the in-plane normal yield stress, $2\sigma_{33}^y > \sigma_{11}^y = \sigma_{22}^y$, and proposed a quartic yield surface to circumvent this limitation. Tensile tests of FRP composites generally register a much smaller yield strength in the transverse direction, governed by the matrix strength and delamination, than they do in the in-plane principal directions. The Hill yield surface will therefore fail to capture the low transverse tensile strengths of FRP composites. The significance of this shortcoming in computations of ballistic impacts has yet to be determined.

UNCLASSIFIED

4.0 Summary and Conclusions

This report documents the development of a material model in EPIC that is orthotropic in its elasticity, plasticity and failure. The model has been developed to simulate the loading to failure of fiber-reinforced polymer composites. Plasticity is characterized by the Hill yield function, and failure is indicated when any component of the material's plastic natural-strain tensor reaches its user-supplied critical value.

The elastic-plastic stress update was implemented using both forward-Euler and backward-Euler finite-difference schemes in time. Although the forward-Euler scheme is explicit, example computations uncovered a maximum timestep that is significantly less than the maximum timestep required by the equations of motion – i.e., the Courant condition. On the other hand, the iterative backward-Euler scheme was stable in all of the example computations when the timestep was governed by the Courant condition. In addition, an initial estimate of the solution to the iterative scheme was found that proved reliable and efficient. As a result, the backward-Euler scheme has demonstrated superior performance, and it has been implemented in the production version of EPIC.

Computations were performed to demonstrate the effects of the model parameters, and for an initial assessment of the model's applicability to composites. Tensile tests on FRP composites demonstrate nearly linear behavior to failure when the direction of loading is aligned with one of the principal material directions, but much greater strains to failure and nonlinearity when the direction of loading deviates from the principal material directions. Computations with the new orthotropic model were shown to reproduce this behavior when the model constants were chosen to reflect greater stiffness and less ductility in the principal material directions.

Computations of the ballistic limits of orthotropic targets were included to demonstrate the model's abilities and potential shortcomings in ballistic applications. The computations identified the components of yield stress that limit the ballistic performance of the example configuration and material parameters. An additional observation was that the Hill yield function requires that no normal yield stress be less than half the other normal yield stresses. This restriction may pose a limitation to the model for some impact configurations and composite materials. However, in many instances the transverse shear stresses allow delamination before the transverse normal yield stress is reached. As a result, the practical significance of the restriction in the disparity of normal yield stresses has yet to be determined. A second potential shortcoming of the Hill yield function is the equivalence of tensile and compressive yield stresses.

As more laboratory and ballistic test data become available, further evaluation of the new orthotropic model will be possible. This may lead to modifications or refinements in its form. Potential improvements include: modification of the form of the failure criteria; addition of an optional yield surface; and transformation to a Total Lagrangian formulation, with its precise treatment of orthotropy in the presence of finite shearing deformations. Finally, the insight gained from meso-scale computations can also be used to improve the homogenized orthotropic model, or to substitute for missing test data when orthotropic model parameters are sought for specific materials.

UNCLASSIFIED

5.0 Acknowledgement

The author would like to thank Drs. Charles Anderson Jr., Sidney Chocron, Alexander Carpenter and Gordon Johnson (all SwRI) for helpful discussions in composite modeling that lead to the orthotropic model in EPIC.

UNCLASSIFIED

UNCLASSIFIED

6.0 References

1. G. R. Johnson, "Numerical algorithms and material models for high-velocity impact computations." *International Journal of Impact Engineering* **38** (2011) pp. 456-472, doi: 10.1016/j.ijmpeng.2010.10.017.
2. G. R. Johnson, S. R. Beissel and P. M. Cunniff, "A computational approach for composite materials subjected to ballistic impact," in Proc. 2nd International Conference on Structural Stability and Dynamics, Dec. 16-18, 2002, Singapore.
3. J. K. Chen, F. A. Allahdadi, C. T. Sun, "A quadratic yield function for fiber-reinforced composites," *Journal of Composite Materials* **31**, No. 8 (1997), pp. 788-811, doi: 10.1177/002199839703100803.
4. J. Cho, J. Fenner, B. Werner and I. M. Daniel, "A constitutive model for fiber-reinforced polymer composites," *Journal of Composite Materials* **44**, No. 26 (2010) pp. 3133-3150, doi: 10.1177/0021998310371547.
5. H. Espinosa, H.-C. Liu, P. Zavattieri and S. Dwivedi, "A 3-D Finite Deformation Anisotropic Visco-Plastic Model for Fiber Composites," *Journal of Composite Materials* **35**, No. 5 (2001), pp. 369-410.
6. C. T. Key, R. W. Six, A. C. Hansen, "A three-constituent multicontinuum theory for woven fabric composite materials," *Composite Science and Technology* **63** (2003), pp. 1857-1864.
7. J. K. Dienes, "On rotation and stress rate in deforming bodies," *Acta Mechanica* **32**, 1979.
8. Ch. E. Anderson, Jr., P. A. Cox, G. R. Johnson and P. J. Maudlin, "A constitutive formulation for anisotropic materials suitable for wave propagation computer programs – II," *Computational Mechanics* **15**, 1994.
9. R. Hill, "The mathematical theory of plasticity" (1950) Oxford University Press, London.
10. P. J. Maudlin and S. K. Schiferl, "Computational anisotropic plasticity for high-rate forming applications," *Computer Methods in Applied Mechanics and Engineering* **131** (1996), pp. 1-30.
11. L. Malvern, *Introduction to the Mechanics of a Continuous Medium*, Prentice-Hall 1969, Englewood Cliffs, N.J.
12. G. R. Johnson and W. H. Cook, "A constitutive model and data for metals subjected to large strains, high strain rates, and high temperatures," Proc. 7th International Symposium on Ballistics, The Hague, Netherlands, April 1983.
13. J. D. Walker and B. H. Thacker, "Yield surfaces for anisotropic plates," Proc. Shock Compression of Condensed Matter – 1999, American Institute of Physics, eds. M. D. Furnish, L. C. Chhabildas, and R. S. Hixson (2000), pp. 567-570.